Temperature estimation of a receiver equipped with a 3D compound parabolic concentrator

Kory Faye[1*], Ababacar Thiam[1, 2], Mactar Faye[1, 2], Ken J. Craig[3], El hadji I. Cissé[2], Vincent Sambou[2]

[1]Research group, Energetic System and Efficiency, Department of Physics, Alioune Diop University, Bambey, Senegal

[2]Laboratory of Water, Energy, Environment and Industrial Processes, Polytechnic School, Cheikh Anta Diop University, Dakar, Senegal

[3]Department of Mechanical and Aeronautical Engineering, University of Pretoria, Pretoria 0002 South Africa

*Corresponding author: kory.faye@uadb.edu.sn

Abstract

Solar Tower Power Plant (STPP) require a high concentration ratio to provide high working fluid temperatures for power generation. Three-dimensional Compound Parabolic Concentrator (3D-CPC) can be used to increase the concentration ratio in the receiver. This paper estimates the air outlet temperature of an indirectly irradiated solar receiver equipped with a 3D-CPC for STPP. For this purpose, the STPP subsystems such as the heliostat field, the 3D-CPC and the receiver are sized for an electrical power of 30 kW. An in-house Matlab code is developed and executed the configuration of the heliostats in the field. The result of the Monte Carlo ray tracing (MCRT) method is used to provide boundary conditions to the Computational Fluids Dynamics (CFD) model. The CFD model is used to simulate the conjugate heat transfer in the receiver. Based on this, a heat source is created from the solar rays absorbed in the receiver. This heat source is implemented as a volumetric heat source in Ansys Fluent by UDFs functions. Thus, the in-house Matlab code is validated by simulating the PS-10 heliostat field and the CFD model is also validated by simulating the Weizmann heliostat field. The results show that the solar field is consisted of 175 heliostats of 2 m^2 surface area and 1.5 m height each. The 3D-CPC truncated at 35° increased the concentration ratio by a factor of 4.91 for an optical efficiency of 80.66%. A receiver mesh count of 1,076,958 gave convergence of the air outlet temperature. $1.5x10^6$ rays are found to get independence of the absorbed heat flux in the receiver. The temperature found on the heated solid is 1063.4 K. For a porosity of 56.02% and a mass flow rate of 0.11 kg/s, a temperature of 1218 K is reached at the outlet of the receiver. The results show that the use of a 3D-CPC increase the concentration ratio and, consequently improve the thermal performance of the receiver. It is important to note that, parameters such as mass flow rate and porosity have a strong influence on the air outlet temperature.

Keywords: CFD, Indirectly irradiated solar receiver, Ray tracing, STPP, UDF, 3D-CPC

Nomenclature

Latin symbols

A_t	total reflecting surface of heliostat (m^2)
A_i	interfacial surface area (m^2)
A_{el}	surface of a mesh element (m^2)
a_1	semi-minor axis of the field (m)
a_2	semi-major axis of the field (m)
$\vec{C}$	target vector of heliostat
d_s	safety distance of heliostats (m)
D_{cav}	diameter of the cavity (m)
d_p	diameter of pores (m)
f_h	heliostat width-to-length ratio
T	temperature (K)
V_t	total volume of porous medium (m^3)
$\vec{V}_n$	normal vector of mesh element
V_p	volume of pores (m^3)
z_m	heliostat height from the base (m)

Greek symbols

α_{3D-CPC}	tilt angle of 3D-CPC (°)
ΔR_{max}	maximum radial spacing (m)
ΔR_{max}	maximum radial spacing (m)
θ_a	half acceptance angle of 3D-CPC (°)

f_{3D-CPC}	focal distance of 3D-CPC (m)	η_{th}	thermal efficiency of receiver
F	inertial resistance coefficient (m^{-1})	η_{conv}	conversion efficiency of turbine C30
h_T	height of the tower (m)	η_{opt}	optical efficiency of the heliostat field
H_h	height of the heliostat (m)	γ_j	angular direction for group j (radians)
k_a	thermal conductivity of air (W/(m.K))	Ψ_m	angular direction (radians)
K	viscous resistance coefficient (m^2)	β_L	tilt angle of the field (°)
k_{SiC}	thermal conductivity of SiC (W/(m.K))	ε	porosity
L_{3D-CPC}	length of the full 3D-CPC (m)	ϕ_T	3D-CPC truncation angle (°)
$L_{3D-CPC,T}$	length of the 3D-CPC truncated (m)	**Abbreviations**	
L_h	length of heliostat (m)	CSP	Concentrating Solar Power
N_i	nodes of i mesh element	CD	Characteristic Diameter (m)
$\vec{n}$	normal vector	CFD	Computational Fluid Dynamics
P_{ray}	power per ray (W)	DNI	Direct Normal Irradiation (W/m^2)
P_e	nominal electrical power (W)	DO	Discrete Ordinates
$R_{i,j}$	radius of ring i in group j (m)	GHG	GreenHouse Gases
r_{in}	inlet aperture radius (m)	UDS	User Define Scalar
r_{out}	outlet aperture radius (m)	UDF	User Define Functions
$r_{in,T}$	inlet aperture radius truncated (m)	UDM	User Define Memory
R_{coef}	optimized coefficient of radius	MCRT	Monte Carlo ray tracing
$\vec{S}$	sun vector	RPC	Reticulate Porous Ceramic
$t_{p.m}$	thickness of the porous medium (m)	STPP	Solar Tower Power Plant
t_{hs}	thickness of the heated solid (m)	3D-CPC	3D Compound Parabolic Concentrator

1. Introduction

Electricity is a vital factor answerable for the economic development of countries. In the 21st century, electricity is considered to be one of the major challenges facing every country. Most of the electricity consumed today (about 80%) comes from the combustion of fossil energy sources [1]. However, the increased use of fossil energy sources for electricity generation results in GreenHouse Gas (GHG) emissions [2]. The GHGs lead to global warming and consequently to rain scarcity, dryness, poverty, etc. In order to reduce the use of fossil energy sources, and thus mitigate its negative effects, the use of renewable energy sources is becoming the best solution [3]. Solar energy is considered one of the main renewable energy sources due to its abundance, cleanliness and positive impact on the environment [4, 5]. The solar energy source can be used for the electrical generation by Concentrating Solar Power (CSP) technologies [6, 7]. Among the CSP technologies, Solar Tower Power Plant (STPP) is considered the most promising for electricity generation [8, 9].

In STPP, the receiver plays a key role [10]. It collects and converts solar rays into thermal energy via the Heat Transfer Fluid (HTF). Thus, improving the receiver thermal performance is equivalent to increasing the performance of the STPP. Among the factors that can improve the receiver thermal performance, we can quote the use of Three-dimensional Compound Parabolic Concentrator (3D-CPC). Indeed, the 3D-CPC allows to reduce the inlet aperture of the receiver, and consequently increases the concentration ratio [11]. The 3D-CPC is also used to eliminate the solar tracking device in polar heliostat field [12].

The STPP equipped with 3D-CPC have been studied experimentally by some researchers. For example, Li et al. [13] made an experimental study on a 3D-CPC for high temperature applications, powered by radiation from a multi-source solar simulator. They showed that the 3D-CPC increases the concentration ratio by a factor of 4.1 at an optical efficiency of 85.4% and reduces spillage losses from 78.9% to 32.1%. Pozivil et al. [14] experimentally investigated the performance of a volumetric pressurized air solar receiver equipped with a 3D-CPC for a

Brayton cycle. The receiver consists of a cylindrical SiC cavity surrounded by a Reticulate Porous Ceramic (RPC) foam contained in a stainless-steel pressure vessel. The 3D-CPC is incorporated into the inlet aperture of the receiver without a transparent window. For a solar radiative of 47 kW, the results showed an air outlet temperature of 1200 °C for an average solar concentration ratio of 2500 suns and a thermal efficiency of 91% at 700 °C and 4 bars. Li et al. [15] studied the energy and economic performance of a STPP equipped with a 3D-CPC. Using Monte Carlo ray tracing (MCRT) method, a heat transfer model and a cost model based on the System Advisor Model (SAM), they showed that a 3D-CPC can improve the energy and economic performance of systems only at temperatures between 900 K and 1200 K.

The combination of rays tracing and CFD has been used by various researchers to investigate the temperature distribution on receivers and their performance. For example, Craig et al. [16] studied the heat losses of a tubular cavity receiver of a parabolic dish at different inclination angles and wind speeds. They used CFD to simulate the heat transfer from the absorbed solar radiation to the HTF. The results showed that 40-50% of the absorbed solar energy was transferred to the HTF for orientations ranging from -45° to 45° and wind speeds between 0.5 m/s and 4 m/s. Moghimi et al. [17] presented a new computational approach using the Finite Volume (FV) method in CFD solver Ansys Fluent to perform the required ray tracing and quantify the optical performance of a linear solar receiver. Garbrecht et al. [18] investigated the performance of the receiver using CFD simulations coupled with solar radiation and heat transfer in molten salt. For an incident solar radiation of 1 MW/m^2, the results showed a thermal efficiency of 91.2%. The reflection and emission losses are reduced to 1.3% and 2.8%, respectively. Ndiogou et al. [19] studied the heat transfer inside the absorber of a volumetric receiver. A numerical model of the cavity-absorber block is proposed with the coupling of the radiation method using infinitesimal zones and CFD code. The good ability of the receiver to transfer heat to the air was proven with a thermal efficiency of 92%. The optimization results showed that the most influential parameter on the outlet temperature is the porosity. Daabo et al. [20] studied different configurations of open cavity solar receivers, including cylindrical, conical and spherical. They used ray tracing and CFD to reduce optical and thermal losses and maximize the exit temperature of the working fluid. The effects of coil pitch and tube diameter on the working fluid's exit temperature are also investigated. The results showed that for a coil pitch value of 3 mm and a tube diameter of 10 mm, the outlet temperature is 401.3 K, 405.7 K and 409.4 K for each respective geometry.

To the best of our knowledge, no work has been published on the numerical design of a 3D-CPC at the receiver inlet i.e., at the top of the tower. In addition, most works using CFD have studied heat transfer by imposing a constant heat flux at the receiver inlet. Which does not correspond to the real heat flux concentrated by the heliostats field and therefore does not reflect reality. In this paper, a 3D-CPC is used to increase the concentration ratio in the receiver. A CFD model is used to simulate the conjugate heat transfer of the absorbed solar rays to the HTF. To achieve these objectives, the heliostat field is sized for an electrical power of 30 kW. An in-house Matlab code is developed and executed the heliostats configuration in the field. The 3D-CPC is sized and designed. The result from the MCRT method is used to provide boundary conditions to CFD model for the simulation of the conjugate heat transfer in the receiver. Thus, the in-house Matlab code is validated by simulating the PS-10 heliostats field and the CFD model is also validated by simulated the Weizmann heliostats field. The results of different investigations are presented and discussed, with conclusion completing the paper.

2. Materials and Methods

2.1. System description

The system described in Fig. 1 is the solar flied model of the STPP consisting of the heliostat field, the tower, the 3D-CPC and the receiver. The 3D-CPC is incorporated at the receiver inlet to reduce its inlet aperture and widen its projection onto the heliostat field. Thus, it increases the concentration ratio in the receiver. The coordinates of the solar field are defined at the center of the tower. The positive x-axis is directed along the heliostat field, i.e., to the South, and the positive y-axis is pointing to the East. The tilt angle (α_{3D-CPC}) of the 3D-CPC is defined as the angle between the line through its center and the z-axis. The half acceptance angle (θ_a) of the 3D-CPC is defined as the maximum angle that allows the incident rays at its inlet aperture to be reflected back to the receiver [15]. Design parameters such as the height (h_T) of the tower, the total reflecting surface area (A_t) of the heliostats, the tilt angle and the half acceptance of the 3D-CPC are determined.

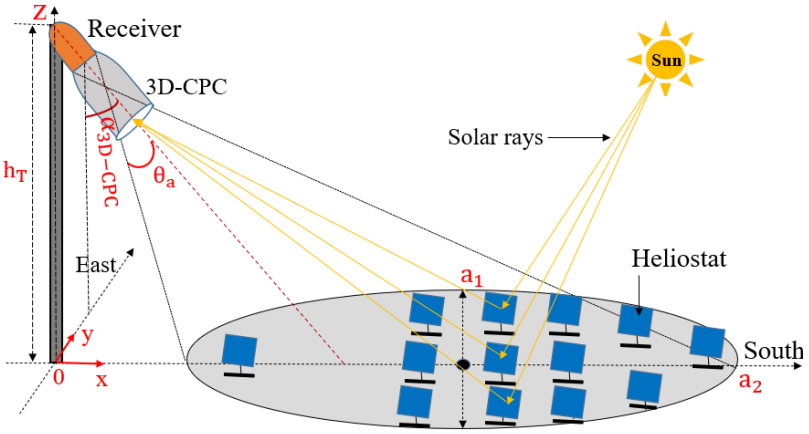

Fig. 1. Solar field model of the STPP equipped with a 3D-CPC

2.1.1. Heliostat field sizing

For sizing the heliostat field, it is important to determine the total reflecting surface area (A_t) of the heliostats. The surface area can be calculated by Eq. (1) [21].

$$A_t = \frac{P_e}{\eta_{opt}.\eta_{th}.\eta_{conv}.DNI} \quad (1)$$

where η_{opt} is the optical efficiency of heliostat field, η_{th} is the thermal efficiency of the receiver, η_{Con} is the electrical efficiency of the system and DNI is the Direct Normal Irradiation.

2.1.2. Heliostat layout design

The heliostat field contributes around 50% of the total cost of the STPP and 40% of the overall energy losses [22]. Therefore, a best layout of heliostats reduces the energy losses and, consequently improves the performance of the STPP. In this work, the radial stagger layout design like PS-10 is used to distribute the heliostats in the field. This layout reduces blocking and shading losses ($\eta_{bl\&sh}$) and represents the most commonly layout used in STPP [23]. The boundaries of the heliostat field shown in Fig.1, depend on the height of the tower and the 3D-CPC inlet shape. The inlet shape of the 3D-CPC is circular and therefore the boundaries of its projection onto the heliostat field are described by an ellipse. Thus, the semi-minor axis (a_1) and the semi-major axis (a_2) of this ellipse are given by Eqs. 2(a) and 3(b) [24]:

$$a_1 = \frac{h_T.\tan(\theta_a).(1+\tan^2(\theta_a))}{1-\tan^2(\alpha_{3D-CPC}).\tan^2(\theta_a)} \quad (2a)$$

$$a_2 = \frac{h_T.\tan(\theta_a)}{1-\tan^2(\alpha_{3D-CPC}).\tan^2(\theta_a)}.\sqrt{(1+\tan^2(\alpha_{3D-CPC}).(1+\tan^2(\alpha_{3D-CPC}).\tan^4(\theta_a))} \quad (2b)$$

In the radial stagger layout, the heliostats are divided into group j, themselves distributed into rings i numbered from the tower, as shown in Fig. 2. This layout takes into account the tilt angle (β_L) of the field. The heliostat trajectory is represented by a circle. Thus, the Characteristic Diameter (CD) is calculated according to the geometric sizes of the heliostat [25].

$$CD = \left(\sqrt{1 + f_h^2} + ds\right).L_h \quad (3)$$

where d_s is the inter-heliostats safety distance, L_h is the length of the heliostat and f_h is the ratio between the width and the length of the heliostat.

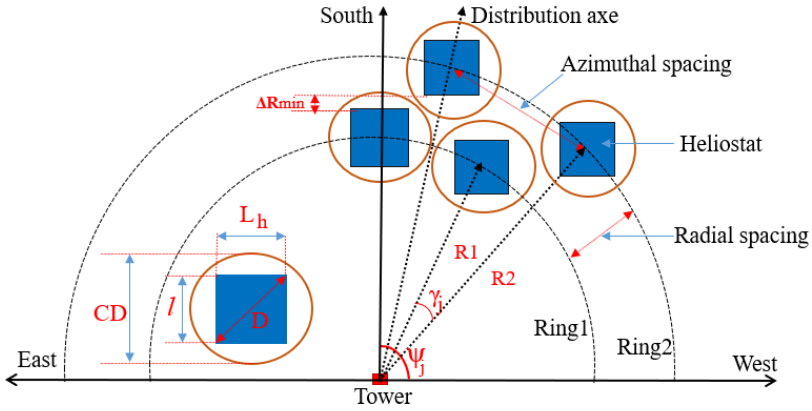

Fig. 2. Parameters defining the heliostats layout design in the field

2.1.2.1. Azimuthal spacing

In the first ring, the azimuthal spacing of each group is equal to CD. In the other rings, the azimuthal spacing is chosen by respecting the no-blocking principal. For any ring, i in a group, j, it is calculated by Eq. (4) [26]:

$$\gamma_j = \frac{CD}{2.R_{i,j}} \quad (4)$$

where $R_{i,j}$ is the radius between the tower and ring i of group j.

Heliostats with the same azimuth angle belong to the same group. Therefore, the angular direction (Ψ_m) defined as the angle between the North axis and the two distribution axes East and West, is given by Eq. (5) [26].

$$\Psi_m = \pm n.\gamma_j \quad (5)$$

where n=0, 2, 4, …for even rings, n=1, 3, 5, … for odd rings, + for the South-East half field, and – for the South-West half field.

2.1.2.2. Radial spacing

The radius of each ring is determined according to its membership. Thus, the radius (R_1) of the first ring depends on the tower height. Collado and Turegano [27] proposed values of the first radius between $h_T/2$ and h_T. In this study, we propose the relation of Eq. (6) to calculate the first radius.

$$R_1 = \frac{h_T}{2} + 1 \quad (6)$$

The radius (R_2) of the second ring in any group, can be determined by Eq. (7) [28]:

$$R_2 = R_1 + CD.\cos(30).\cos(\beta_L) \quad (7)$$

where β_L is the tilt angle of the field.

The minimum radial spacing (ΔR_{min}) between the heliostats can be calculated by Eq. (8) [28].

$$\Delta R_{min} = CD.\cos(30).\cos(\beta_L) \quad (8)$$

To calculate the maximum radial spacing (ΔR_{max}) given by Eq. (10), the no-blocking principle between adjacent heliostats must be respected. The parameters of this principle are calculated by Eqs. 9(a); 9(b) and 9(c) [29].

$$z_m = R_1 . \tan(\beta_L) + H_h \quad (9.a)$$

$$d = \sqrt{R_1^2 + (h_T - z_m)^2} \quad (9.b)$$

$$\gamma = \arcsin\left(\frac{CD}{2.d}\right) + \arcsin\left(\frac{R_1}{d}\right) - \beta_L \quad (9.c)$$

$$\Delta R_{max} = \frac{CD . \cos(\beta_L)}{\cos(\gamma)} \quad (10)$$

Thus, the radius of the third, fourth, and i rings can be calculated by Eq. (11) [29].

$$R_{1+i} = R_1 + \Delta R_{min} + R_{coef} . (\Delta R_{max} - \Delta R_{min}) \quad (11)$$

where R_{coef} is the optimized coefficient of the radius ($0< R_{coef} <1$).

2.1.2.3. Heliostat orientations

The first step before determining the orientations of the heliostats, is to find the position of the Sun. The coordinates of the Sun are calculated by the system of Eq. (12) [30].

$$S = \begin{cases} S_x = \cos(\alpha) . \sin(A) \\ S_y = \cos(\alpha) . \cos(A) \\ S_z = \sin(A) \end{cases} \quad (12)$$

where α is the altitude of the Sun and A is azimuth angle of the Sun.

The angular direction (Ψ_m) and the radius of each ring (R_i) calculated previously allow the heliostat positions in the field. The position of each heliostat is calculated by the system given by Eq. (13) [29].

$$H = \begin{cases} H_x = R_i . \sin(\Psi_m) \\ H_y = R_i . \cos(\Psi_m) \\ H_z = H_h \end{cases} \quad (13)$$

The normal vector ($\vec{n}$) of the heliostat depends on the Sun vector ($\vec{S}$) and the vector ($\vec{R}$) located between a heliostat and the receiver. It can be determined by Eq. (14) [31].

$$\vec{n} = \frac{\vec{R} + \vec{S}}{\sqrt{2.(1 + \vec{S}.\vec{R})}} \quad (14)$$

The target vector ($\vec{C}$) determining the orientation of each heliostat is given by Eq. (15) [31].

$$\vec{C} = \vec{H} + \vec{n} \quad (15)$$

2.1.3. 3D-CPC sizing

The two parameters defining the 3D-CPC geometry are the half acceptance angle (θ_a) and the inlet aperture radius (r_{in}). The half acceptance angle is the angle between the 3D-CPC optical axis (z) and the line (AB), as shown in Fig. 3. Therefore, solar rays with incidence angles greater than θ_a do not reach the receiver. From these parameters, the outlet aperture radius (r_{out}) and the length (L_{3D-CPC}) of the 3D-CPC are calculated by Eqs. 16(a) and 16(b), respectively [32].

$$r_{out} = r_{in} . \sin(\theta_a) \quad (16.a)$$

$$L_{3D-CPC} = \frac{f_{3D-CPC} . \cos(\theta_a)}{\sin^2(\theta_a)} \quad (16.b)$$

where f_{3D-CPC} is the focal distance of the 3D-CPC, given by the following expression [32]:

$$f_{3D-CPC} = r_{out} . (1 + \sin(\theta_a)) \quad (16.c)$$

As can be seen in Fig. 3, the upper part of the 3D-CPC is almost parallel to the optical axis (z). Consequently, this part contributes to a very low concentration of solar rays. Therefore, for reasons of efficiency, economy and lightness, this part is truncated. The truncation changes the field of view of the 3D-CPC and allows some solar rays, beyond the half acceptance angle, to reach the receiver [33]. Thus, the inlet aperture radius ($r_{in,T}$) and the length ($L_{3D-CPC,T}$) of the 3D-CPC truncated are calculated by Eqs. 17(a) and 17(b), respectively [34].

$$r_{in,T} = \frac{f_{3D-CPC} \cdot \sin(\phi_T - \theta_a)}{\sin^2(\phi_T/2)} - r_{out} \quad (17.a)$$

$$L_{3D-CPC,T} = \frac{f_{3D-CPC} \cdot \cos(\phi_T - \theta_a)}{\sin^2(\phi_T/2)} \quad (17.b)$$

where ϕ_T is the truncation angle

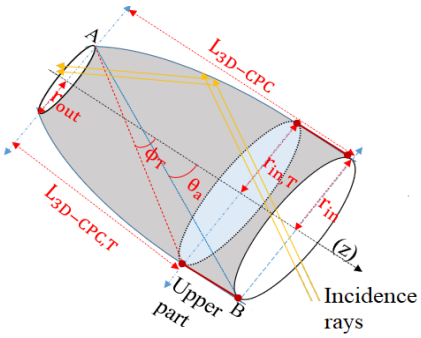

Fig. 3. Geometrical description of the 3D-CPC

2.1.4. 3D-CPC design method

Designing a 3D-CPC using optical modelling tools such as SolTrace has been problematic for a long time because of its complex geometric shape. However, the team of K.J. Craig [35] have developed a method to design a complex solar receiver in SolTrace. This method consists of producing a meshed receiver with elements that have associated centroids and aim point coordinates. To adapt this method in this work, the geometric shape of the 3D-CPC is at first designed in SolidWorks. Then, it is meshed in Ansys Meshing with a triangular mesh element to avoid overlapping elements causing blocking and shading. After meshing, two files, one containing the elements and their nodes (N_1, N_2, N_3) and the other containing the nodes and their coordinates (x, y, z), are extracted. Thus, the centroid coordinates of each element are calculated by taking the average of the three node coordinates of each element. To calculate the coordinates of the aim points, it is necessary to determine the normal vector coordinates of each element. Eq. 18(a) is used to calculate the coordinates of each element after translation [16].

$$\begin{pmatrix} x \\ y \\ z \end{pmatrix}_{NiG} = \begin{pmatrix} x \\ y \\ z \end{pmatrix}_{OG} - \begin{pmatrix} x \\ y \\ z \end{pmatrix}_{Ni} \quad (18.a)$$

By choosing two nodes (e.g., N_1, and N_2), the normal vector coordinates of each mesh element are calculated by the cross product of its two nodes.

$$\vec{v}_n = (y_1z_2 - z_1y_2)\vec{i} + (z_1x_2 - x_1z_2)\vec{j} + (x_1y_2 - y_1x_2)\vec{k} \quad (18.b)$$

Eq. 18(c) is used to calculate the aim points coordinates (A_P) of each mesh element [16].

$$\begin{pmatrix} x \\ y \\ z \end{pmatrix}_{Ap} = \begin{pmatrix} x \\ y \\ z \end{pmatrix}_{OG} + \begin{pmatrix} x \\ y \\ z \end{pmatrix}_{Vn} \quad (18.c)$$

By doing this, the 3D-CPC can be modelled as set of separate elements in SolTrace, using the built-in irregular triangle option.

2.2. Operating parameters

2.2.1. Receiver description

The geometry of the indirectly irradiated solar receiver is shown in Fig. 4. It consists of three domains: the cavity, the heated solid and the porous medium. The cavity length (L_{cav}) is 0.5 m, the cavity diameter (D_{cav}) is 0.5 m, the inlet aperture diameter (D_{in}) is 0.25 m, the porous medium thickness ($t_{p.m}$) is 0.1 m and the heated solid thickness ($t_{h.s}$) is 0.01 m. These sizes were obtained in our previous study [36, 37]. The values of pressure, mass flow rate, and temperature of the pressurized air at the inlet of the receiver are 0.35 MPa, 0.11 kg/s, and 300 K, respectively [38]. The 3D-CPC is incorporated into the receiver inlet aperture to reduce the size and consequently increase the concentration ratio. The solar rays concentrated in the cavity are absorbed by the heated solid. Thus, the absorbed heat is transferred by radiation and convection to the pressurized air flowing through the porous medium.

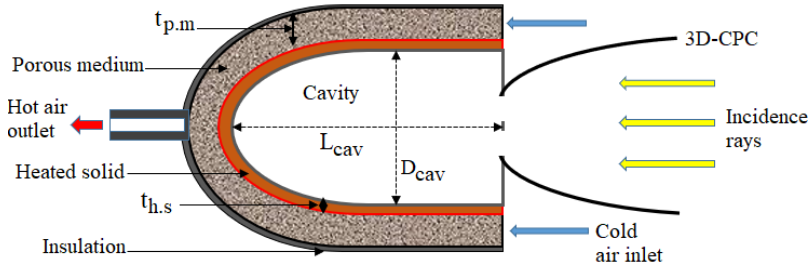

Fig. 4. Description of the indirectly irradiated solar receiver

2.2.2. Sizing parameters

The capstone gas turbine (C30) was assumed to be the electrical conversion system of the STPP. These characteristics showed in Table 1, are used for the sizing of the heliostat field. Other parameters such as a DNI of 600 W/m^2, an optical efficiency (η_{opt}) of 76.4%, a tower height (h_T) of 26 m and a receiver thermal efficiency (η_{th}) of 80% found in our previous study [37], are also used in this work.

Table 1. Sizing parameters of the heliostat field [39].

Parameters	Values	Units
Nominal electrical power	30	[kW]
Electrical efficiency	0.26(±2)	[-]
Turbine inlet temperature	1173	[K]
Pressure ratio	3.45	[-]
Exhaust gas temperature	548	[K]
Electrical generator	0.90	[-]

2.2.3. Numerical procedure

The flow chart in Fig. 5 describes the procedure for converting the solar rays concentrated by the heliostat field into thermal energy to heat air flow in the porous medium. The procedure consists of four steps:

- The first step is devoted to the MCRT method. Based on this, the heliostats concentrated solar rays into the 3D-CPC. Solar rays undergo several reflections inside the 3D-CPC before being transferred to the receiver. For this process, the full 3D-CPC is truncated at different truncation angles. At each truncation angle, solar flux is collected until the value of solar flux (F_i) is greater than the solar fluxes (F_{i-1}) and (F_{i+1}). Thus, the solar flux of the optimal truncation is used for the volumetric heat source.

- The second step is devoted to the volumetric heat source obtained by converting the solar flux absorbed in the receiver. For this, the ray count (hit) that fall on receiver mesh element is multiplied by the power per ray (P_{ray}) and divided by the element surface (A_{el}) to obtain the heat source in 2D. This heat source is then divided by the heated solid thickness ($t_{h.s}$) which gives the volumetric heat source in 3D. Eq. (19) is used to calculate the volumetric heat source. Thus, the volumetric heat source is used to create an interpolation file (*. ip file) which will be interpolated on the heated solid by UDFs functions. (See the *. ip file format in the appendix, line 123 to 135).

$$H_s = (\text{hit}.P_{ray})/(A_{el}.t_{h.s}) \quad (19)$$

- The third step is dedicated to set the parameters, the materials properties and boundary conditions if all domains in section 2.2.4, and the governing equations in section 2.2.5 in Ansys Fluent.
- Once Ansys Fluent is configured, the fourth step is dedicated to the interpolation of the volumetric heat source on the solid heated by the UDFs functions. The steps of the interpolation are summarized in Fig. 5 (see the details of interpolation and the UDF code in the appendix, line 76 to 121).

It should be noted that the solution converges for any mesh of the receiver. However, it might not converge accurately, which affects the results obtained. As thus, to have precise results, a mesh dependency study according to the air outlet temperature of the receiver is necessary. The convergence to the desired accuracy is guaranteed when the difference of the air outlet temperature is less than or equal to 2% [40].

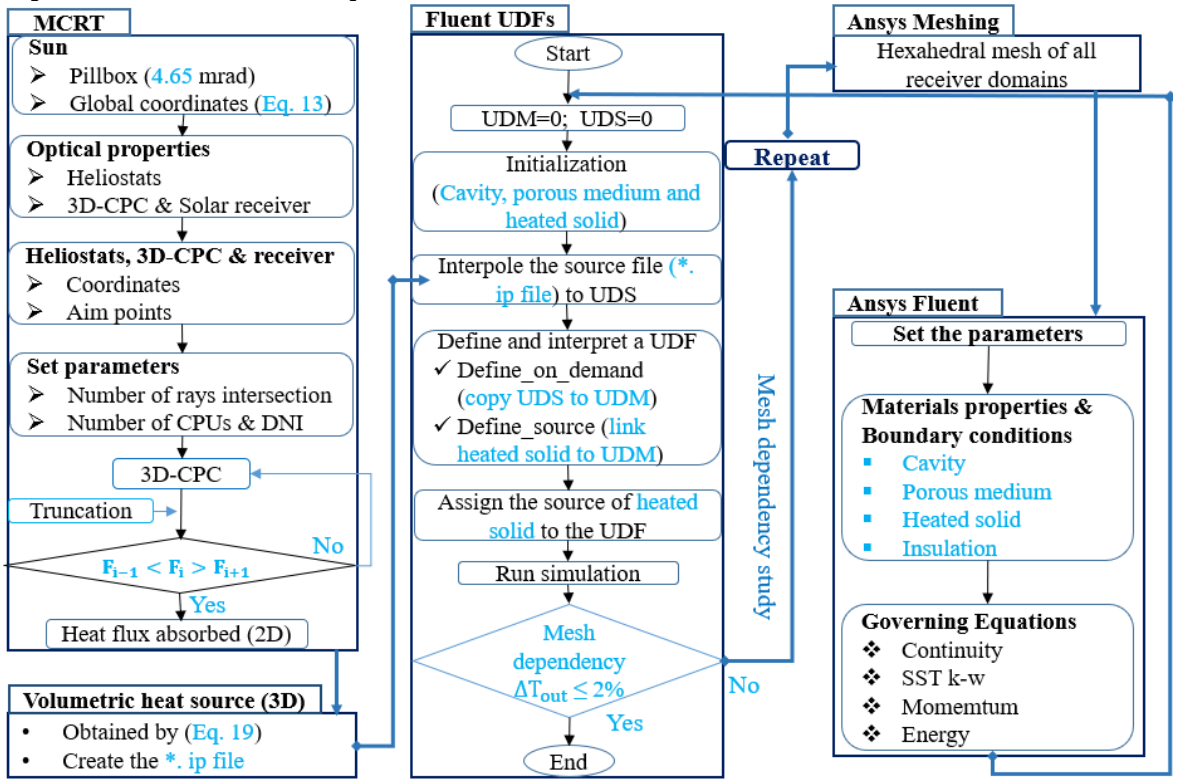

Fig. 5. Flow chart of numerical procedure for coupled ray tracing and CFD

2.2.4. Material properties and boundary conditions

The thermal properties of the materials used in each domain of the receiver are shown in Table 2. The heated solid and the porous matrix are made of silicon carbide (SiC), which has a relatively high thermal conductivity and reasonable thermal stress resistance at high

temperatures [41]. Due to the elevated temperatures in the receiver, the thermal conductivities of the air (k_a) flowing through the porous medium and the silicon carbide (k_{SiC}) are given by the Eqs. 20(a) and 20(b), respectively [42].

$$k_a = -3.94.10^{-4} + 1.02.10^{-4}T + 4.86.10^{-8}T^2 + 1.52.10^{-11}T^3 - 6.12.10^{-18}T^4 \quad (20.a)$$

$$k_{SiC} = 203.1 - 0.4176T + 4.365.10^{-4}T^2 + 2.2.10^{-7}T^3 + 4.232.10^{-11}T^4 \quad (20.b)$$

Air is assumed to be transparent to solar radiation and the effect of convective heat transfer on solar radiation should only be considered during conjugate heat transfer in the porous medium. Thus, the air inside the cavity is modelled as a solid transparent to solar radiation (with an absorption coefficient of 0) and having the thermal properties of air. This favours that only the radiative transfer and energy transfer equations must be solved in this domain (i.e., in the cavity). To limit the re-radiations in the cavity, the opaque walls of the domain are modelled as being cold with a specified temperature of 1 K [17]. The porous medium is assumed to be a uniform and isotropic. The porous medium is treated as radiatively participating medium. It takes into account the propagation and absorption of concentrated solar rays. These radiative characteristics depend also on the porosity (ε) and the viscous (K) and the inertial (F) resistance coefficients given by Eqs 21(a), 21(b) and 21(c), respectively [43]. The regime is assumed to be permanent. The airflow is assumed to be incompressible, turbulent and two-dimensional [19]. The outlet boundary was set with a static pressure of 0 Pa. The thermal boundaries in the adjacent walls of the domains are coupled. All the external boundaries of the receiver except the inlet air are made of stainless-steel material like [16].

$$\varepsilon = {V_p}/{V_t} \quad (21.a)$$

$$K = \frac{\varepsilon^3 d_p^{0.264}}{1.36.10^8(1-\varepsilon)^2} \quad (21.b)$$

$$F = {A_p}/{V_t} \quad (21.a)$$

Table 2. Materials properties used in the different domains of the receiver [44, 45, 46]

Domains	Parameters	Values	Units
Porous medium (Fluid)	Density	Incompressible-ideal-gas	[kg/m^3]
	Thermal capacity	1006.43	[J/(kg.K)]
	Thermal conductivity	(Eq. 20(a))	[W/ (m.K)]
	Viscosity	1.7894.10^{-5}	[kg/ (m.s)]
Cavity (Solid)	Density	1.2	[kg/m^3]
	Thermal capacity	871	[J/(kg.K)]
	Thermal conductivity	0.02	[W/ (m.K)]
	Emissivity	0.9	[-]
Heated solid (Solid)	Density	3170	[kg/m^3]
	Thermal capacity	871	[J/(kg.K)]
	Thermal conductivity	(Eq. 20(b))	[W/ (m.K)]
	Absorption coefficient	0.93	[m^{-1}]

2.2.5. Computational settings in Fluent

A hexahedral mesh was used for the receiver, as show in Fig. 13. Dense meshes were generated in the walls of the heated solid where the temperature is higher. The three-dimensional conjugate heat transfer problem is solved using Ansys Fluent v2020R2 [47]. We have chosen the SST k-w turbulence model for the turbulent closure of the Reynolds-averaged steady-state

Navier-Stokes equations. The solution is double precision using the segregated coupled solver in Ansys Fluent. The Discrete Ordinates (DO) model is used to calculate the thermal re-radiation with 3 x 3 angular discretization and 3 x 3 pixelation [48]. The spatial discretization of the pressure, momentum, energy, and discrete ordinate equations are chosen as second order, ascending second order, second order upwind and first order upwind, respectively.

3. Results and discussion

3.1. Validation

3.1.1. In-house Matlab code validation

The in-house Matlab code for the optical model is validated by simulating the PS-10 heliostat field with the listed parameters in the Table 3. Fig. 6 shows the predicted radiative flux distributions on the receiver surface. A good agreement was found between our in-house Matlab code and the code developed by Li et al. [15] with a percentage error of 3.7% (see the coordinates of the PS-10 heliostat in Fig. A.1 and the details of the validation in the appendix, line 4 to 14).

Table 3. Validation parameters of the in-house Matlab code [15]

	Parameters	Values
Sun	Site: Barstow, CA, USA	5116'56', N34°53'
	Position	7:30 Am, June 20th
Heliostat	Size	10 m x 10 m, single facet
	Slope error	2 mrad
	Reflectance	0.95
Receiver	Height	62 m
	Aiming point	(0, 0, 62)
	Aperture	6 m x 8 m
	Absorptance	0.90

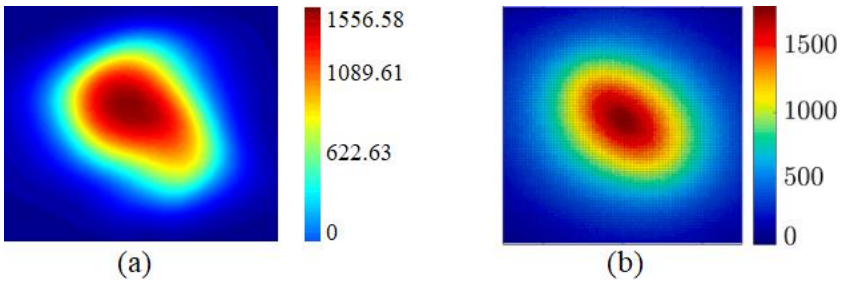

Fig. 6. Flux distribution in the receiver: (a) in-house Matlab code and, (b) Li et al. [15].

3.1.2. CFD model validation

The CFD model developed is validated by simulating the Weizmann heliostats field [41, 49]. Indeed, it is the only STPP equipped with a 3D-CPC. The validation parameters of the CFD model are presented in Table 4. The same procedure described in the flow chart of Fig. 5 is used for the CFD validation. For this, the air outlet temperature is determined as a function of the air mass flow rate like Pozivil et al. [14]. The result obtained is shown in Fig. 7. A good agreement is found between the present model and the experimental model of Pozivil et al. [14]. The difference between the air outlet temperature gave a coefficient of determination of R^2=0.98. This proves that the CFD model developed is satisfactory for analyzing the heat transfer coupled with the solar flux inside the receiver. (See details of the CFD model validation in the appendix, line 15 to 48)

Table 4. Validation parameters of the CFD model [41, 49]

	Parameters	Values	Units
Site	Latitude	31° 54' 40" N	[-]
	Longitude	34° 49' 5" E	[-]
	Time zone	UTC + 2:00	[-]
	DNI	911	[W/m^2]
Heliostat	Number	4	[-]
	Sizes	7.84 x 7.85	[m]
Tower	Height	30.4	[m]
Receiver	Cavity length	500	[mm]
	Cavity inner diameter	250	[mm]
	Cavity wall thickness	7	[mm]
3D-CPC	Inlet aperture diameter	634	[mm]
	Outlet aperture diameter	147	[mm]
	Acceptance angle	12	[°]
	Tilt angle from the horizontal	26.6	[°]
	Tilt angle towards North-East	23.6	[°]

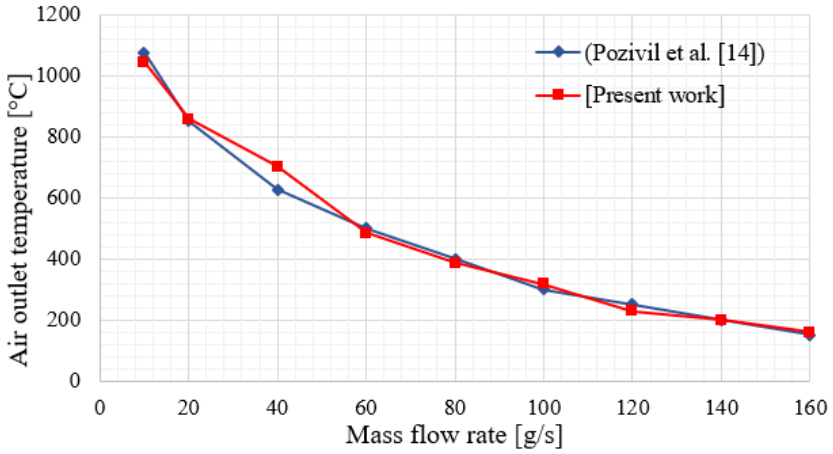

Fig. 7. Air outlet temperature as a function of the air mass flow rate

3.2. Heliostat sizing and layout results

From the parameters quoted in section 2.2.2 and in Table 1, the total reflecting surface area of the heliostats is 350 m^2. The heliostats used in STPP such as PS-10 and Khi Solar One are large in size (121 m^2 and 128 m^2, respectively) [50]. Indeed, the large size of the heliostats makes maintenance and upkeep difficult and thus increases the costs of implementation. In view of this, we have chosen heliostat of 2 m^2 surface area and 1.5 m height, which are easy to handle for maintenance and upkeep. Base on this, the solar field consists 175 heliostats. The heliostats are placed to the South of the tower, as show in Fig. 8. For an inter-heliostat safety distance (ds) of 0.3, the CD of the heliostats is equal to 2.42 m. The minimum (ΔR_{min}) and maximum (ΔR_{max}) radial spacings between the heliostats are 2.10 m and 2.45 m, respectively for an optimized coefficient of radius (R_{coef}) of 0.6 [51]. After calculating the parameters, the in-house Matlab code is implemented to distribute the heliostats in the field. The surface of the field is assumed to be horizontal, and therefore it tilt angle (β_L) is equal to 0°. The heliostat field consists of 14 rings divided into 7 even and 7 odd rings. The distances of the first and last rings are14 m and 42.33 m, respectively.

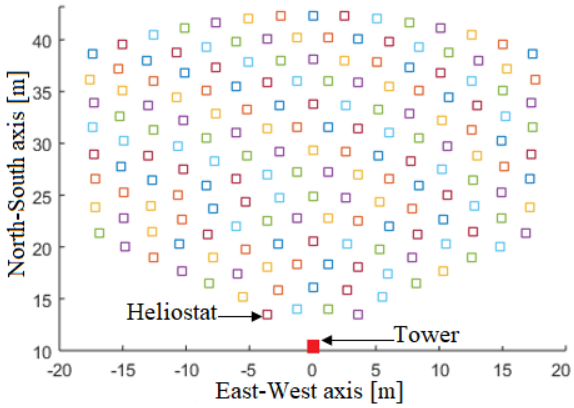

Fig. 8. Staggered radial heliostat layout design in the field

3.3. 3D-CPC sizing and design results

The basic geometrical sizes of the 3D-CPC, namely a half acceptance angle (θ_a) of 12.5° and an inlet aperture radius (r_{in}) of 0.70 m, are determined by optical simulations. From these values, the length (L_{3D-CPC}) and the outlet aperture radius (r_{out}) of the 3D-CPC are 3.84 m and 0.15 m, respectively. Based on this, the geometrical shape of the 3D-CPC is at first designed in SolidWorks v18, as shown in Fig. 9(a). Then, the 3D-CPC is meshed in Ansys Meshing, as shown in Fig. 9(b). At last, the Fig. 9(c) shows the 3D-CPC designed in SolTrace.

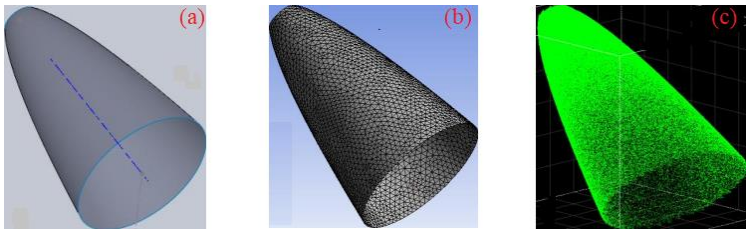

Fig. 9. 3D-CPC: (a) designed in SolidWorks, (b) meshed in Ansys Meshing and (c) designed in SolTrace

3.4. STPP modelling in SolTrace

Among the optical modeling tools, we used SolTrace v2012.12.7 to design the STPP. SolTrace was developed by the National Renewable Energy Laboratory (NREL) and is freely available on their website. It uses the MCRT method [52]. In order for the solar field to be designed and simulated in SolTrace, the simulation parameters, the sizes of the STPP subsystems, and the DNI must be well-defined. These parameters are shown in Table 5. Note that the same method developed in section 2. 1. 4 to design the 3D-CPC, is used to design the receiver. For the sun shape, we chose a pillbox distribution (θ_{Sun}= 4.65 mrad) [53].

Table 5. Characteristics of the STPP subsystems

Subsystems	Parameters	Values	Units
Heliostat	Number	175	[-]
	Surface area	2	[m^2]
	Facets number	1	[-]
	Height	1.5	[m]
	Reflectivity	0.95	[θ]
	Slope error	1	[mrad]
	Specularity error	0.2	[mrad]
Tower	Height	26	[m]
	Half acceptance angle	12.5	[°]
	Tilt angle	50	[°]
	Length	3.84	[m]

3D-CPC	Inlet aperture radius	0.7	[m]
	Outlet aperture radius	0.15	[m]
	Reflectivity	0.96	[θ]
	Slope error	0.6	[mrad]
	Specularity error	0.2	[mrad]
Receiver	Cavity diameter	0.5	[m]
	Cavity length	0.5	[m]
	Aperture diameter	0.25	[m]
	Porous medium thickness	0.1	[m]
	Heated solid thickness	0.01	[m]
	Absorptivity	0.95	[-]

The model of the solar field designed in SolTrace is shown in Fig. 10(a). It consists of the heliostats, the tower, the 3D-CPC and the receiver. The heliostats collect and concentrate the solar rays in the 3D-CPC and the receiver, as show in Fig. 10(b). Due to the multiple reflections of the solar rays in the 3D-CPC (Fig. 10(c)), it increases the concentration ratio inside the receiver, as show in Fig. 10(d).

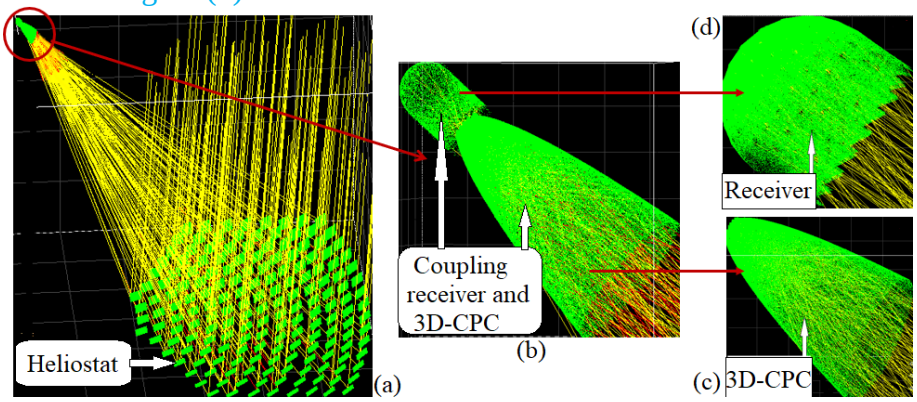

Fig. 10. (a) solar field designed in SolTrace, (b) coupling receiver and 3D-CPC, (c) solar rays' reflections into the 3D-CPC and (d) solar rays absorbed in the receiver

To remove the ambiguity about the mesh elements size of the 3D-CPC, we performed a dependency study. Based on this, the desired number of ray intersections is increased and the average solar flux at the 3D-CPC outlet is collected for mesh elements diameter of 0.001 m, 0.01 m, 0.05 m and, 0.10 m. The simulations are done at 12:00 during the summer solstice (June 21). The results are shown in Fig. 11. It can be seen that by increasing the number of ray intersections, the average solar flux decreases for each size of the mesh elements. The decreasing of the average solar flux is due that when the desired number of ray intersections increase, the solar flux distribution becomes more uniform over the receiver surface, consequently its power decreases. From $1x10^5$ rays onwards, even if the desired number of ray intersections go on to increase, the average solar flux remains constant for each size. Thus, this number of ray intersections can be considered to give a convergence for the value of the average solar flux. Therefore, the 3D-CPC with a mesh element size of 0.01 m is chosen because it gives a higher average solar flux (555.3 kW/m^2) at $1x10^5$ rays.

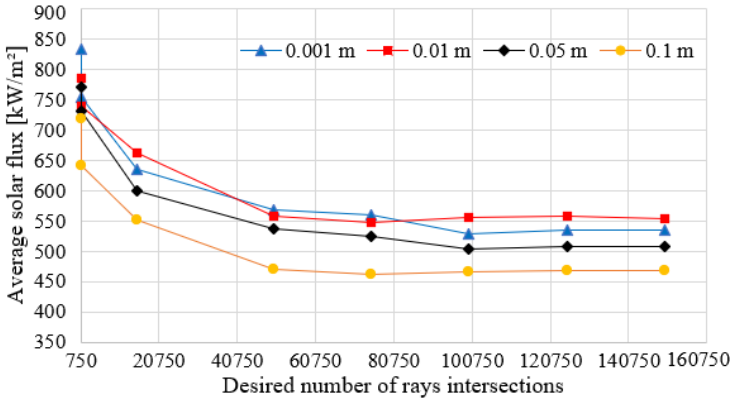

Fig. 11. Mesh elements size dependency of the average solar flux

As pointed out in section 2. 1. 3, the length of the full 3D-CPC (at 3.84 m) is high compared to its inlet aperture diameter (at 1.4 m). Note that the untruncated 3D-CPC has a truncation angle of 25°. Therefore, it is truncated for different truncation angles such as 35°, 40° and 55°. At each truncation angle, the average solar flux is collected until the optimal angle is reached as shown in the flow chart in Fig. 5. The optimal truncation angle gives a higher average solar flux at the 3D-CPC outlet. The results obtained are shown in Table 6. It can be seen that the truncation angle of 35° gives a higher solar flux (574.4 kW/m²). Therefore, the 3D-CPC truncated at 35° with a length of 2.62 m, an inlet aperture radius of 0.68 m and an outlet aperture radius of 0.15 m is used for the subsequent studies. The optical simulations showed that the 3D-CPC truncated at 35° increased the concentration ratio by a factor of 4.91 for an optical efficiency of 80.66% (see details in the appendix line 63 to 75).

Table 6. Sizes and average solar flux obtained for 3D-CPC truncated

Truncation angle [°]	**Length [m]**	**Inlet aperture radius [m]**	**Average solar flux [kW/m²]**
25	3.84	0.70	556.2
35	2.62	0.68	574.4
40	1.88	0.63	539.4
55	1.40	0.58	527.2

3.5. Computational mesh of the receiver

The way the geometry of the solar receiver is designed has a strong influence on the quality meshing and accuracy of the results. For this reason, the receiver geometry is constructed in Ansys SpaceClaim, as shown Fig. 12(a). The three domains of the receiver as mentioned above in section 2.2.1, are showed in Fig.12(b)

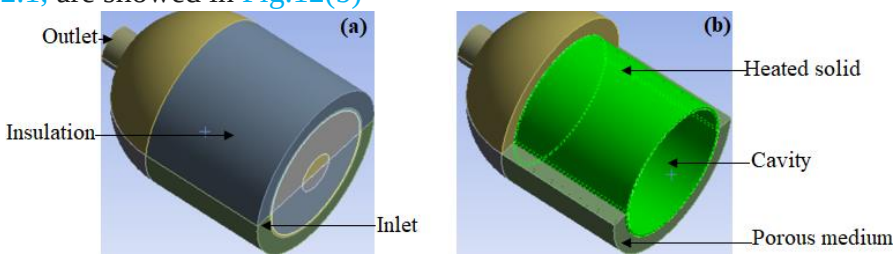

Fig. 12. Indirectly irradiated solar receiver: (a) geometrical form, (b) three domains.

As previously stated, the design of the receiver allowed the use of hexahedral elements for the meshing of all domains. This resulted in a fully mapped mesh with high quality hexahedral elements. Fig. 13(a) shows the receiver meshed. The same number of divisions is imposed on each domain. This makes the mesh finer in the smaller domains, like the heated solid, the porous

medium and the cavity, respectively. Fig. 13(b) shows the side face meshed of the receiver. Fig. 13(c) shows zoom on this face showing the mesh elements of each domain. A mesh dependency study is necessary to find the optimal number of mesh elements, as stipulated in section 2.2.3.

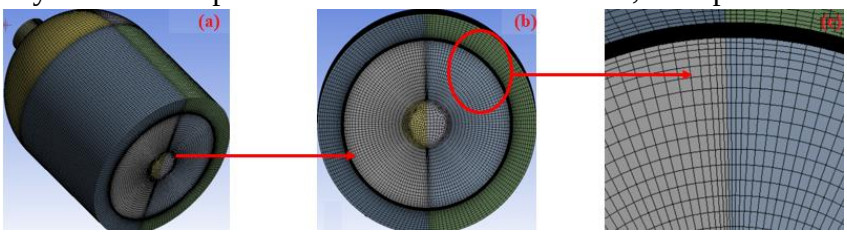

Fig. 13. Mesh of the receiver: (a) all domains, (b) front view, and (c) zoom in on the front.

For the mesh dependency study, the air outlet temperature is determined as a function of the mesh element count. The dependency is studied with a DNI of 1000 W/m², which provides a high air outlet temperature. The set of domains is meshed with mesh elements between 674,502 and 1,378,800. The mesh dependency results found are shown in Table 7. It can be seen that from 976,344 mesh elements onwards, the evolution of the air outlet temperature is almost constant. The difference of the air outlet temperature between 976,344 and 1,076,958 mesh elements is 0.12%. Therefore, the number of 1,076,958 mesh elements of the receiver is adopted in this work.

Table 7. Result of mesh dependency study.

Parameters	**Values**					
Mesh count	674,502	775,116	875,730	976,344	1,076,958	1,378,800
Air outlet temperature [K]	1095.1	1286.0	1355.5	1252.0	1253.5	1238.0

3.6. Interpolation of heat source into CFD model

The solar flux used is obtained from the solar rays concentrated by the heliostat field inside the receiver. During the summer solstice, the solar heat flux is maximum at 12:00 and the average heat flux is 127 kW/m^2. Fig. 14(a) shows the heat flux contours of the heated solid wall. Dividing this value by the thickness of the heated solid gives the average volumetric heat source equal to 12700 kW/m^3. Fig. 14(b) shows the volumetric heat source on the cross section of the heated solid. The local hot spots can be seen in the heated solid wall. Indeed, the hot spots are due to a great concentration of the heat flux on the heated solid wall. It has a negative impact on the solar receiver operation and, consequently decrease its performance [54]. To improve the heat flux distribution on the heated solid wall, a ray and mesh independency study is conducted on the section 3.7.

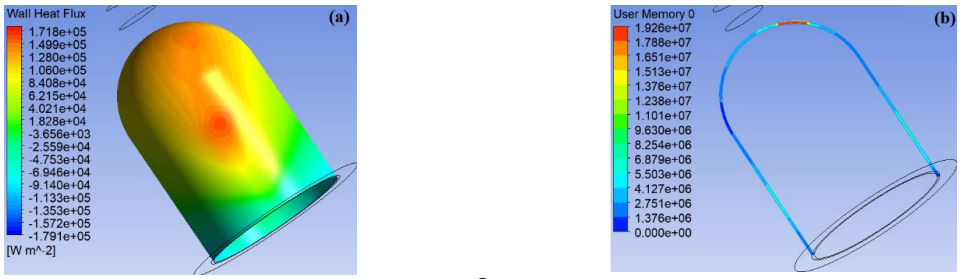

Fig. 14. Heated solid: (a) heat flux (W/m^2) and, (b) volumetric heat source (W/m^3)

3.7. Ray and mesh independency study

The desired number of ray intersections has an influence on the radiative flux density over the heated solid wall. For this purpose, a ray independence study is performed to determine the number of ray intersections that gives a convergent solution. In Fig. 15, the absorbed volumetric heat flux is showed as the desired number of ray intersections is increased. The colors that

appear on the walls of the heated solid show a mesh element that receives a large number of rays. The total heat absorbed for $1.5x10^6$ rays is $9.07x10^8$ W/m^3, while the total heat absorbed for $2x10^6$ rays is $9.08x10^8$ W/m^3, a difference of 0.11%. This result shows that the convergence is obtained at a ray count of $1.5x10^6$. Fig. 16 shows the average absorbed heat flux as function of the desired number of ray intersections. The convergence is more obvious on the average absorbed flux and obtained at a ray count above $1x10^6$. However, to ensure that this number of ray intersections reaches the receiver, we have chosen $1.5x10^6$ rays for the following.

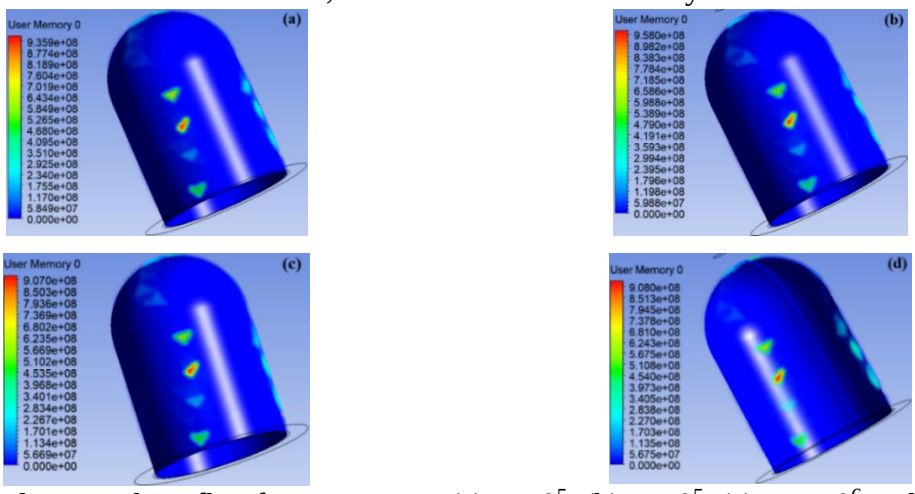

Fig. 15. Volumetric heat flux for ray counts: (a) $1x10^5$, (b) $5x10^5$, (c) $1.5x10^6$ and (d) $2x10^6$ rays

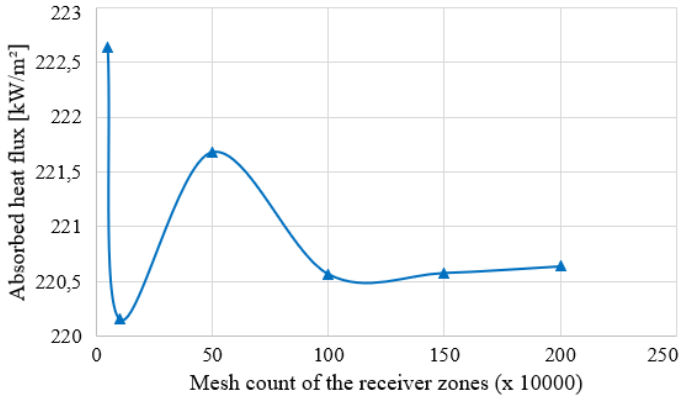

Fig. 16. Convergence of the average heat flux as function of the mesh counts

3.8. Temperature contours of the receiver domains

Fig. 17 shows the temperature contours on the walls of the heated solid. The results show that the temperature varies according to the daily sunshine conditions. The DNI data used in this work are real data measured in Senegal. The location of maximum volumetric heat source on the heated solid corresponds to higher temperatures. Indeed, the orientation of the heliostats from 8:00 am to 6:00 pm strongly influences the way they concentrate solar rays in the 3D-CPC, and consequently in the receiver. This results in a clustering of solar rays in one location and creates a local hot spot on the walls of the heated solid, as shown in Figs. 17(a), 17(b), 17(c) and 17(d). As shown in section 2.2.4, the material of the heated solid is silicon carbide (SiC) which is a good conductor. Thus, it transfers a large part of the heat by conduction to the porous medium where the air considered as the HTF flows. It also transfers heat to the air in the cavity by radiation. The average temperatures of the heated solid are given in Table 8.

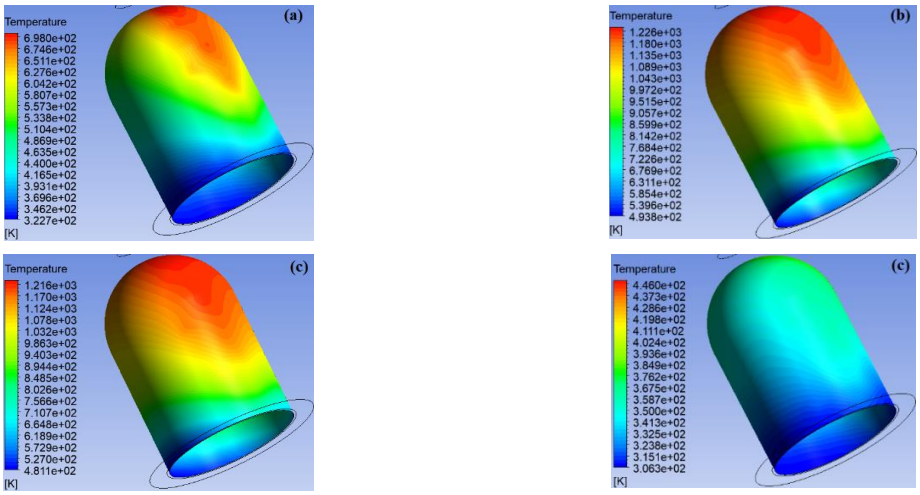

Fig. 17. Heated solid temperature contours at: (a) 8:00, (b) 12:00, (c) 14:00 and, (d) 6:00.

The temperature contours of the air in the cavity are shown in Fig. 18. As stipulate in section 2.2.4, the air in the cavity is modeled as a transparent solid. This facilitates two-way heat transfer from the heated solid. Much of the heat absorbed by the heated solid is transferred into the porous medium. The air in the cavity contributes to the radiation but does not absorb any, so radiation losses in the cavity aperture are reduced. Thus, it is clear that the cavity aperture becomes hotter than the wall sides. This may also be due to the entry of cold air at 300 K into the receiver. Radiation heat losses are expected at the cavity aperture. As is well known, heat tends to move from hot to cold zones. This is clearly noticeable in the Figs. 18(a), 18(b), 18(c) and 18(d) at 8:00, 12:00, 14:00 and, 6:00, respectively. The average temperatures on the wall cavity aperture are given in Table 8.

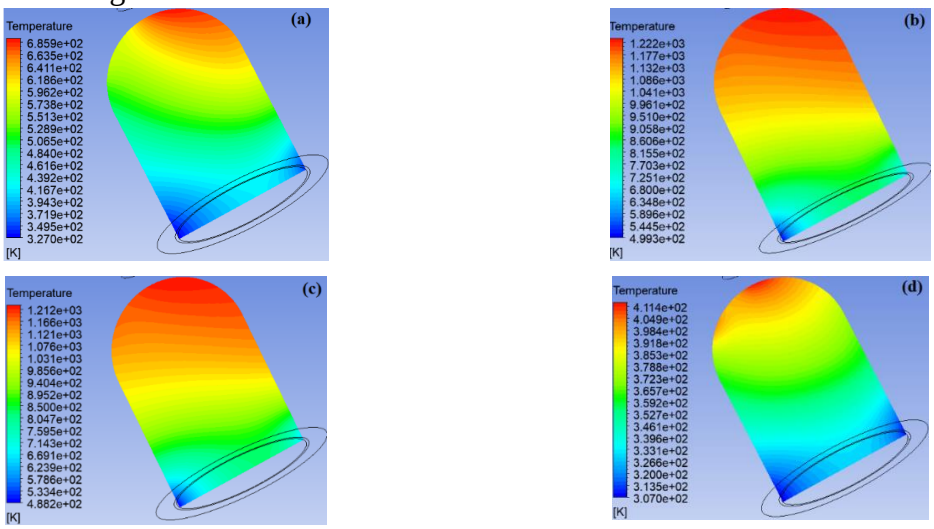

Fig. 18. Cavity temperature contours at: (a) 8:00, (b) 12:00, (c) 14:00 and, (d) 6:00.

The temperature contours of the HTF (air) in the porous medium are shown in Fig.19. The porous medium consists of pores with a porosity of 56.02%. The pressurized air enters with a mass flow rate of 0.11 kg/s, a temperature of 300 K and a pressure of 0.35 MPa. It is heated by the walls of the heated solid as it moves towards to the receiver exit. The small thickness of the heated solid (0.01 m) allows better conduction heat between the heated solid and the porous medium. In addition, heat transfer also occurs by radiation, conduction and possibly convection between the pores of the porous medium. Figs. 19(a), 19(b), 19(c) and 19(d) show the temperature profiles of porous medium at 8:00, 12:00, 14:00 and 6:00, respectively. The air outlet temperatures are given in Table 8.

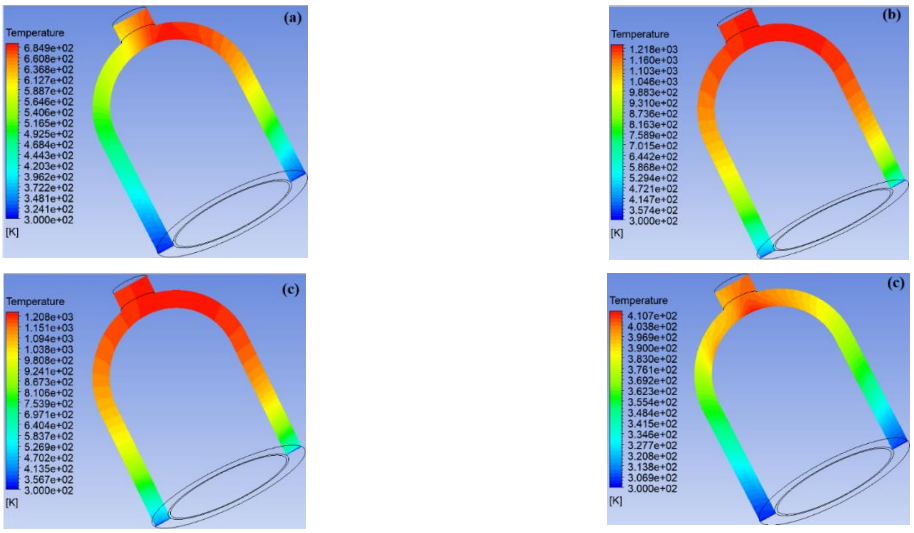

Fig. 19. Porous medium temperature contours at: (a) 8:00, (b) 12:00, (c) 14:00 et (d) 6:00

3.9. Performance of the receiver

The average temperatures of the heated solid, the air outlet, the cavity and the wall cavity aperture of the receiver as function daily conditions are given in Table 8. The evolution of these temperatures is more visible in Fig. 20. The highest temperature on the heated solid is 1063.4 K at 12:00. For a porosity of 56.02% and an inlet air mass flow rate of 0.11 kg/s, the air outlet temperature reaches 1218 K. This shows that the porosity and the imposed mass flow rate, the thermal conductivity and the thickness of the material used in the heated solid are important parameters which improve the thermal performance of the receiver. Furthermore, the maximum temperature at the wall cavity aperture is 744.1 K. The radiation losses at the cavity aperture are also listed in Table 8.

Table 8. Temperatures of all domains and radiation heat losses at the cavity aperture

Times [hours]	8	10	12	14	16	6
DNI [W/m^2]	194.1	413.0	524.4	515.4	409.1	96.0
Heated solid temperature [K]	543.0	884.7	1063.4	1051.3	850.2	369.0
Air outlet temperature [K]	643.4	1051.0	1218.0	1207.5	1014.4	400.5
Air cavity temperature [K]	526.5	859.0	1040.1	1027.6	824,4	364.0
Wall cavity aperture temperature [K]	385.3	569.0	744.1	728.4	543.0	322.2
Radiation losses on cavity aperture [kW]	1.1	4.8	10.1	9.7	4.1	0.1

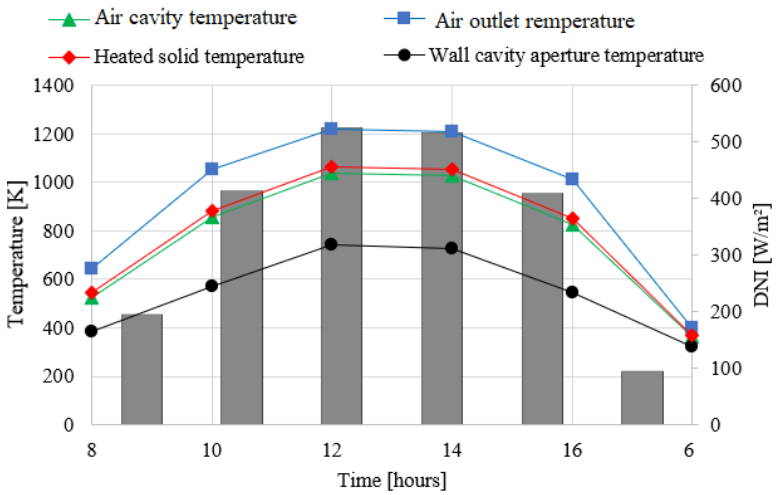

Fig. 20. Average temperatures as a function of daily conditions

4. Conclusion

In this paper, a numerical approach is used to evaluate the air outlet temperature of an indirectly irradiated solar receiver equipped with a Three-dimensional Compound Parabolic Concentrator (3D-CPC) for a Solar Tower Power Plant (STPP). For this purpose, the STPP subsystems are sized for an electrical power of 30 kW. An in-house Matlab code is developed and executed the layout of the heliostats in the field. The result of the Monte Carlo ray tracing (MCRT) method is used to provide boundary conditions to the Computational Fluids Dynamics (CFD) model for the simulation of conjugate heat transfer in the receiver. Based on this, a heat source is created from the solar rays absorbed in the receiver. The heat source is implemented as a volumetric heat source in Ansys Fluent by UDFs functions. Thus, the in-house Matlab code is validated by simulating the PS-10 heliostat field and the CFD model is also validated by simulating the Weizmann heliostat field. The main findings are as follows:

- The solar field consist of 175 heliostats of 2 m^2 surface area and 1.5 m height each.
- The 3D-CPC truncated at 35° increased the concentration ratio by a factor of 4.91 for an optical efficiency of 80.66%.
- A receiver mesh count of 1,076,958 gave convergence of the air outlet temperature. $1.5x10^6$ rays is found to get the independence of the absorbed heat flux in the receiver.
- The temperature found on the heated solid is 1063.4 K. For a porosity of 56.02% and a mass flow rate of 0.11 kg/s, an air temperature of 1218 K is reached at the receiver exist.
- The results show that the use of a 3D-CPC can increase the concentration ratio and therefore improve the thermal performance of the receiver. It is important to note that, parameters such as thermal conductivity, mass flow rate and porosity have a strong influence on the air outlet temperature.

However, the variation in solar flux may result overheating of the 3D-CPC and also the receiver. Overheating influences the operating and the optical performances of the 3D-CPC and consequently those of the receiver. Cooling the 3D-CPC could be a promising solution to overcome the overheating of the 3D-CPC and the receiver.

Declaration of competing interest

The authors declare that they have no known competing financial interests or personal relationships that could have appeared to influence the work reported in this paper.

Acknowledgements

The financial support of the West African Economic and Monetary Union (WAEMU) for research and training (grant no. 0600/2021) is gratefully acknowledged. The authors thank also the academic authorities of the Alioune Diop University of Bambey and Polytechnical School of Dakar for their support.

References

[1] M. Shahabuddin, M. A. Alim, T. Alam, M. Mofijur, S. F. Ahmed, G. Perkins, A critical review on the development and challenges of concentrated solar power technologies, Sustainable Energy Technologies and Assessments, 47 (2021) 101434.

[2] D. Zhao, E. Xu, Z. Wang, Q. Yu, L. Xu, L. Zhu, Influences of installation and tracking errors on the optical performance of a solar parabolic trough collector. Renewable Energy, 94 (2016) 197-212.

[3] K. Wanga, Z. Zhang, M.J. Li, Ch. Min, A coupled optical-thermal-fluid-mechanical analysis of parabolic trough solar receivers using supercritical CO2 as heat transfer fluid, Applied Thermal Engineering, 183 (2021) 116154.

[4] E. Bellos, C. Tzivanidis, Alternative designs of parabolic trough solar collectors, Progress in Energy and Combustion Science, 71 (2019) 81-117.
[5] A. M. Daabo, A. Ahmad, S. Mahmoud, R. K. Al-Dadah, Parametric analysis of small-scale cavity receiver with optimum shape for solar powered closed Brayton cycle applications, Applied Thermal Engineering, 122 (2017) 626-641.
[6] Z.D. Cheng, Y.L. He, K, Wang, B.C. Du, F.Q. Cui, A detailed parameter study on the comprehensive characteristics and performance of a parabolic trough solar collector system, Applied Thermal Engineering, 63 (2014) 278-289.
[7] S. Guillén-Lambea, M. Carvalho, A critical review of the greenhouse gas emissions associated with parabolic trough concentrating solar power plants, Journal of Cleaner Production, 289 (2021) 125774.
[8] K. Milidonis M. J. Blanco, V. Grigoriev, C. F. Panagiotou, A. M. Bonanos, M. Constantinou, J. Pye, C. Asselineau, Review of application of AI techniques to Solar Tower Systems, Solar Energy, 224 (2021) 500-515.
[9] K. Wang, Y. He, Y. Qiu, Y. Zha,g, A novel intergrated simulation approach couples MCRT and Gebhart methods to simulate solar radiation transfert in a solar power tower system with a cavity receiver, Renewable Energy, 89 (2016) 93-107.
[10] S. Wang, C. Asselineau, Y. Wang, J. Pye, J. Coventry, Performance enhancement of cavity receivers with spillage skirts and secondary reflectors in concentrated solar dish and tower systems, Solar Energy, (2020) 708-727.
[11] G. Leveque, R. Bader, W. Lipinski, S. Haussener, High-flux optical systems for solar thermochemistry, Solar Energy, 156 (2017) 133-148.
[12] R. Xu, Y. Ma, M. Yan, C. Zhang, S. Xu, R. Wang, Effects of deformation of cylindrical compound parabolic concentrator (CPC) on concentration characteristics, Solar Energy, 176 (2018) 73-86.
[13] L. Li, B. Wang, J. Pottas, W. Lipiński, Design of a compound parabolic concentrator for a multi-source high-flux solar simulator, Solar Energy, 183 (2019) 805-811.
[14] P. Pozivil, N. Ettlin, F. Stucker, A. Steinfeld, Modular design and experimental testing of a 50 kWth pressurized-air solar receiver for gas turbines, Journal of Solar Energy Engineering, 137 (2015) 031002-1.
[15] L. Li, B. Wang, J. Pye, W. Lipiński, Temperature-based optical design, optimization and economics of solar polar-field central receiver systems with an optional compound parabolic concentrator, Solar Energy, 206 (2020) 1018-1032.
[16] K. J. Craig, M. Slootweg, W.G. Le Roux, T. M. Wolff, J. P. Meyer, Using CFD and ray tracing to estimate the heat losses of a tubular cavity dish receiver for different inclination angles, Solar Energy, 211 (2020) 1137-1158.
[17] M. A. Moghimi, K. J. Craig, J. P. Meyer, A novel computational approach to combine the optical and thermal modelling of Linear Fresnel Collectors using the finite volume method, Solar Energy, 116 (2015) 407-427.
[18] O. Garbrecht, F. Al-Sibai, R. Kneer, K. Wieghardt, CFD-simulation of a new receiver design for a molten salt solar power tower, Solar Energy, 90 (2013) 94-106.
[19] B. A. Ndiogou, A. Thiam, C. Mbow, P. Stouffs, D. Azilinon, Numerical analysis and optimization of an indirectly irradiated solar receiver for a Brayton cycle, Energy, 166 (2019) 519-529.
[20] A. M. Daabo, S. Mahmoud, R. K. Al-Dadah, A. Ahmad, Numerical investigation of pitch value on thermal performance of solar receiver for solar powered Brayton cycle application, Energy, 119 (2017) 523-539.
[21] K.E. N'Tsoukpoe, K. Y. Azoumah, E. Ramde, A. K. Y. Fiagbe, P. Neveu, X. Py, M. Gaye, A. Jourdan, Integrated design and construction of a micro-central tower power plant, Energy for Sustainable Development, 31 (2016) 1-13.

[22] S. M. Besarati, D. Y. Goswami, A computationally efficient method for the design of the heliostatfield for solar power tower plant, Renewable Energy, 69 (2014) 226-232.
[23] Z. A. Hussaini, P. King, Sansom, Numerical simulation and design of multi-tower concentrated solar power fields, Sustainability, 12 (2020) 2-22.
[24] A. Segal, Optimum layout of heliostat field when the tower-top receiver is provided with secondary concentrators, Weizmann Institute of Science, Report for SFERA, WP.13, Task2, (April 2012).
[25] Q. Xie, Z. Guo, D. Liu, Z. Chen, Z. Shen, X. Wang, Optimization of heliostat field distribution based on improved Gray Wolf optimization algorithm, Renewable Energy, 176 (2021) 447-458.
[26] F. M. F. Siala, M. E. Elayeb, Mathematical formulation of a graphical method for a no-blocking heliostat field layout, Renewable Energy, 23 (1) (2001) 77-92.
[27] F.J. Collado, J. A. Turégano, Calculation of the annual thermal energy supplied by a defined heliostat field, Solar Energy, 42 (2) (1989) 149-165.
[28] Ch. Li, R. Zhai, H. Liu, Y. Yang, H. Wu, Optimization of a heliostat field layout using hybrid PSO-GA algorithm, Applied Thermal Engineering, 128, (2018), 33-41.
[29] Y. Zhou, Y. Zhao, Heliostat field layout design for solar tower power plant based on GPU, in Preprints of the 19th World Congress IFAC Cape Town, South Africa, (August 2014).
[30] M. J. Reno, C. W. Hansen, J. S. Stein, Global horizontal irradiance clear sky models: implementation and analysis, Sandia Report SAND2012-2389, National Nuclear Security Administration (2012).
[31] S. M. Besarati, D. Y. Goswami, A computationally efficient method for the design of the heliostat field for solar power tower plant, Renewable Energy, 69 (2014) 226-232.
[32] R. Winston, Principles of solar concentrators of a novel design, Solar Energy, 16 (1974) 89-95.
[33] S. S. Indira, C. A. Vaithilingam, R. Sivasubramanian, K. Chong, R. Saidur, K. Narasingamurthi, Optical performance of a hybrid compound parabolic concentrator and parabolic trough concentrator system for dual concentration, Sustainable Energy Technologies and Assessments, 47 (2021) 101538.
[34] E. Leonardi. Detailed analysis of the solar power collected in a beam-down central receiver system, Solar Energy, 86 (2012) 734-745.
[35] M. Slootweg, K. J. Craig, J. P. Meyer, A computational approach to simulate the optical and thermal performance of a novel complex geometry solar tower molten salt cavity receiver, Solar Energy, 187 (2019) 13-29.
[36] B. A. Ndiogou, A. Thiam, C. Mbow, M. I. S. Adjibade, V. Sambou, Modeling and optimization method of an indirectly irradiation solar receiver, MethodsX, 6 (2019) 43-55.
[37] K. Faye, A. Thiam, M. Faye, Optimum height and tilt angle of the solar receiver for a 30 kWe solar tower power plant for the electricity production in the Sahelian zone, International Journal of Photoenergy, (2020) ID 1961134.
[38] A. M. Daabo, A. Al Jubori, S. Mahmoud, R. K. Al-Dabah, Development of three-dimensional optimization of a small-scale radial turbine for solar powered Brayton cycle application, Applied Thermal Engineering, 111 (2017) 718-733.
[39] M. C. Cameretti, Modelling of a hybrid solar micro-gas turbine fuelled by biomass from agriculture product, Energy Reports 6 (2020) 105-116.
[40] Z.D. Cheng, Y.L. He, F.Q. Cui, Numerical investigations on coupled heat transfer and synthetical performance of a pressurized volumetric receiver with MCRT-FVM method, Applied Thermal Engineering, 50 (2013) 1044-1054.
[41] P. Pozivil, S. Ackermann, A. Steinfeld, Numerical heat transfer analysis of a 50 kWth pressurized-air solar receiver, Journal of Solar Energy Engineering, 137 (2015) 064504-1.

[42] Z. Wu, Z. Wang. Fully coupled transient modeling of ceramic foam volumetric solar air receiver, Solar Energy, 89 (2013) 122-133.
[43] J. Petrasch, F. Meier, H. Friess, A. Steinfeld, Tomography based determination of permeability, Dupuit-Forchheimer coefficient, and interfacial heat transfer coefficient in reticulate porous ceramics, International Journal of Heat and Fluid Flow, 29 (2008) 315-326.
[44] S. Shoeibi, H. Kargarsharifabad, S.A.A. Mirjalily, M. Sadi, A. Arabkoohsar. A comprehensive review of nano-enhanced phase change materials on solar energy applications, Journal of Energy Storage, 50 (2022) 104262.
[45] R. Pérez-Álvarez. P.A. González-Gómez, D. Santana, A. Acosta-Iborra. Preheating of solar power tower receiver tubes for a high-temperature chloride molten salt, Applied Thermal Engineering, 216 (2022), 119097
[46] J. Cabrero, F. Audubert, R. Pailler, A. Kusiak, J.L. Battaglia, P. Weisbecker, Thermal conductivity of SiC after heavy ions irradiation, Journal of Nuclear Materials, 396 (2010) 202-207.
[47] Ansys: https://www.ansys.com/resource-center/webinar/ansys-2020-r2-ansys-fluent, available online.
[48] K. Craig, M. Moghimi, A. Rungasamy, J. Marsberg, J. Meyer, Finite-volume ray tracing using computational fluid dynamics in linear focus CSP applications, Applied Energy, 183 (2016) 241-256.
[49] P. Pozivil, On-sun demonstration and heat transfer analysis of a modular pressurized air solar receiver, ETH Zurich Research Collection, https://doi.org/10.3929/ethz-a-010610153 (2015).
[50] J. B. Blackmon, Heliostat size optimization for central receiver solar power plants, Concentrating Solar Power Technology, Woodhead Publishing Series in Energy, (2012) 536-76.
[51] M. Atifa, F. A. Al-Sulaiman. Optimization of heliostat field layout in solar central receiver systems on annual basis using differential evolution algorithm, Energy Conversion and Management, 95 (2015) 1-9.
[52] T. Wendelin, A. Dobos, SolTrace: a ray-tracing code for complex solar optical systems. Tech. Rep. NREL/TP-5500–59163, National Renewable Energy Laboratory, Golden, CO (2013).
[53] Y. Wang, D. Potter, Ch-A. Asselineau, C. Corsi, M. Wagner, C. Caliot, B. Piaud, M. Blanco, J-S. Kim, J. Pye, Verification of optical modelling of sunshape and surface slope error for concentrating solar power systems, Solar Energy, 195 (2020) 461-474.
[54] Y. Ch. S. Too, J. García, R. V. Padilla, J-S. Kim, M. Sanjuan, A transient optical-thermal model with dynamic matrix controller for solar central receivers, Applied Thermal Engineering, 154 (2019) 686-698